GALACTIC CHEMICAL EVOLUTION

SAMPLE PAPERS

Timmes et al. 1995 ApJS 98 617

* Goswami & Prantzos 2000 A&A 359 191

Kobayashi et al. 2006 ApJ 653 1145

ISOTOPES → 2011 MNRAS 414 3231

G+P /2000 : Cu to Zn

- **INGREDIENTS**

– n'synthesis

MASSIVE STARS (SN II)

– how many choices

– integrate over IMF

(i) C, N, O, Ne, and Mg are mainly produced in hydrostatic burning phases. They are mostly found in layers which are not heavily processed by explosive nucleosynthesis. The yields of these elements depend on the pre-supernova model (convection criterion, mixing processes, mass loss and nuclear reaction rates).

(ii) Al, Si, S, Ar and Ca are also produced by hydrostatic burning, but their abundances are subsequently affected by the passage of the shock wave. Their yields depend on both the pre-supernova model and the shock wave energy.

(iii) Fe-peak elements as well as some isotopes of lighter elements like Ca, S and Ti are produced by the final SN explosion (SN II). Their yields depend crucially upon the explosion mechanism and the position of the "mass-cut".

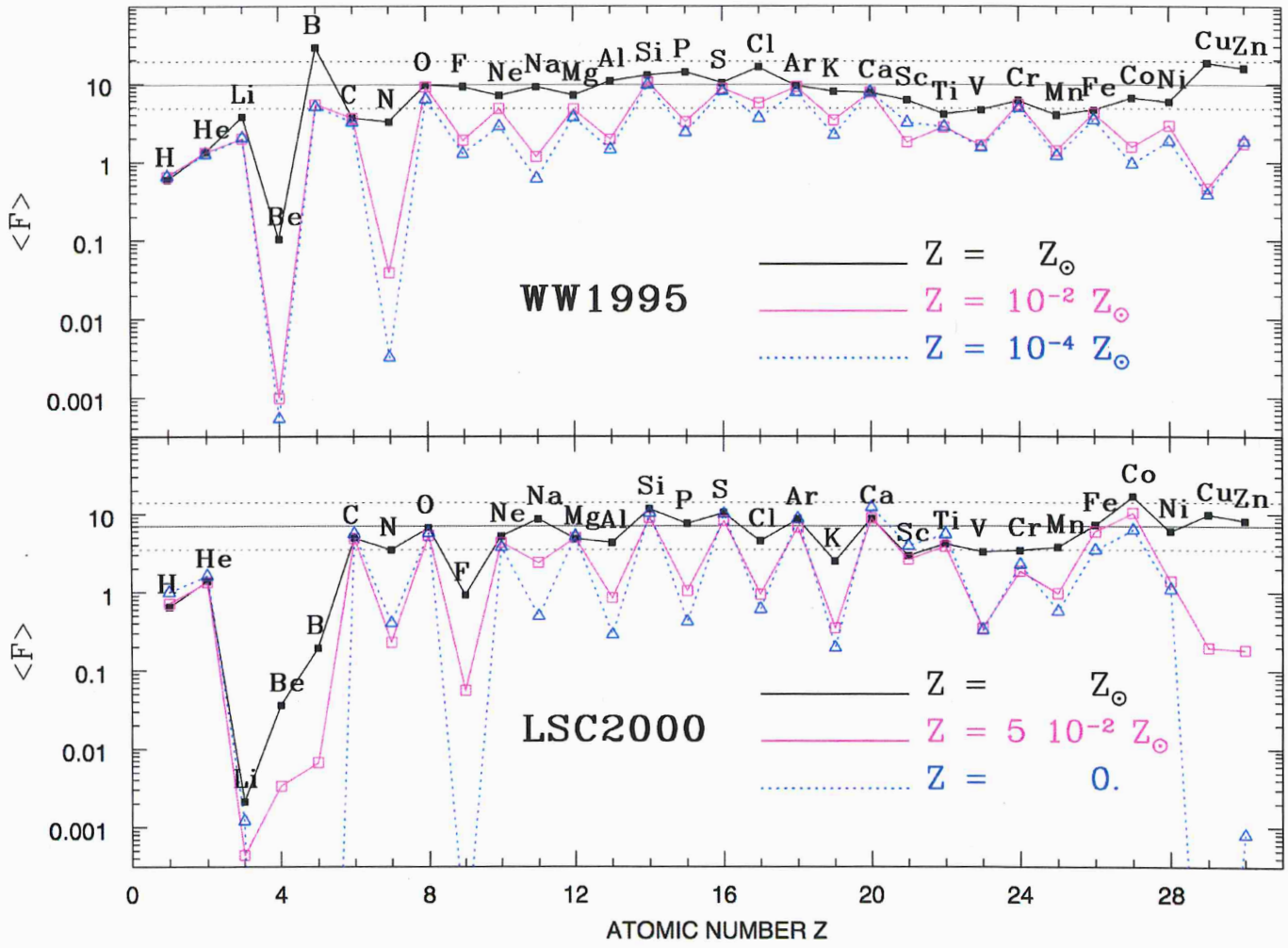

Fig. 1. Average overproduction factors (over a Kroupa et al. (1993) IMF, see Eq. 1) of the yields of Woosley & Weaver 1995 (WW1995, *upper panel*) and Limongi et al. 2000 (LSC2000, *lower panel*) for 3 different initial stellar metallicities. In both cases, the *solid horizontal lines* are placed at F_{oxygen} and the two *dotted horizontal lines* at half and twice that value, respectively. The "odd-even effect" is clearly seen in both the data sets. N behaves as a pure "secondary". The elements He, C, N, Li and Be in both cases (as well as B and F in LSC2000) require another production site

- Type Ia SN
  - updated W7 model
    Z=Z⊙ and Z=0 models
    (interpolated linearly)

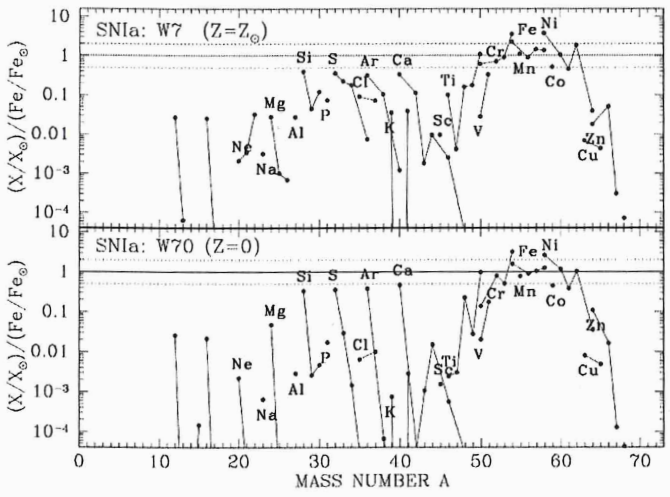

Fig. 2. Isotopic yields of SNIa resulting from Chandrasekhar mass white dwarfs, according to Iwamoto et al. (1999). *Top panel:* model W7 (the white dwarf results from a star of initial metallicity Z=Z□). *Bottom panel:* model W70 (the white dwarf results from a star of initial metallicity Z=0). Both models are calculated with updated nuclear reaction rates (with respect to the "old" W7 model of Thielemann et al. 1986). In both cases, the overproduction factor of ^{56}Fe is taken as 1, while variations by a factor of 2 are indicated by *dotted* lines. ^{54}Cr and ^{58}Ni are clearly overproduced in those models

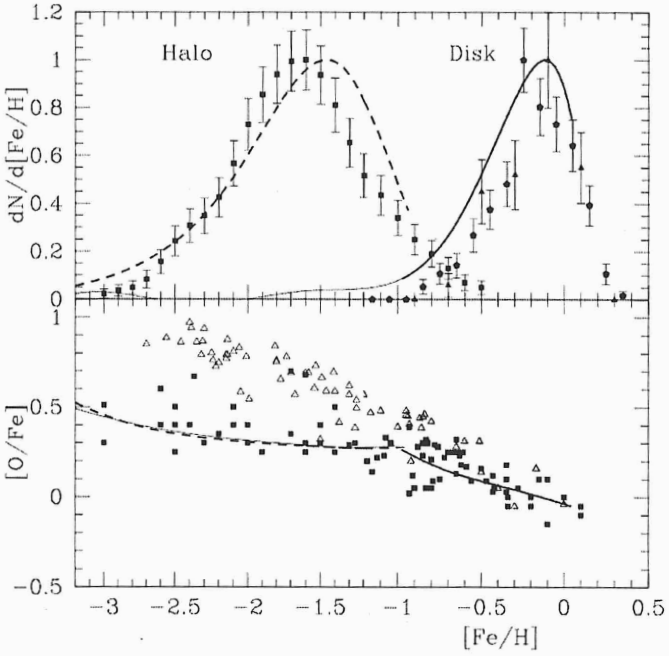

Fig. 3. *Upper panel*: Model metallicity distributions (MD) of the galactic halo (*dashed curve*) and the local disc (*solid curve*) obtained with appropriate models and the metallicity dependent yields of WW1995; The "traditional" disk population, at [Fe/H]> -1, is indicated by a *thick* curve (see Sect. 4.1). Observations for halo MD are from Norris & Ryan (1991, *filled squares*) and for the disk from Wyse & Gilmore (1995, *filled pentagons*) and Rocha-Pinto & Maciel (1996, *filled triangles*). *Lower panel*: [O/Fe] vs. [Fe/H] in the halo (*dashed curve*) and the disk (*solid curve*, *thick* for [Fe/H]> -1 and *thin* for [Fe/H]< -1), according to our model. Observed abundances are from sources listed in Table 1 (*filled squares*), except for those of Israelian et al. (1998) and Boesgaard et al. (1999) (*open triangles*). All MDs are normalised to $f_{max}=1$

GALACTIC MODEL

- no mixing between zones
- Instant. Recycling, Approx (IRA)
- stellar lifetimes & remnant masses
- SFR / IMF
- Infall / Outflow
- Halo & Disk separately

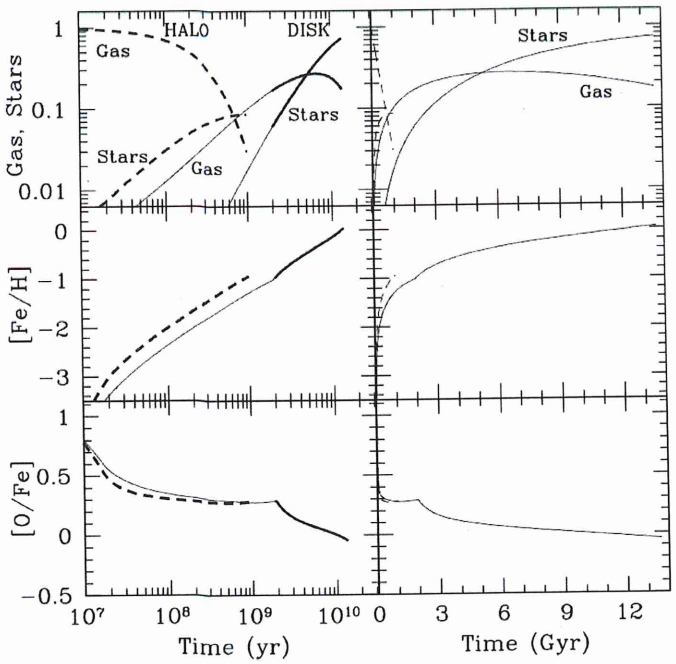

Fig. 4. Evolution of stars, gas and metals in our models for the halo and the disk, plotted as a function of time. A logarithmic time scale is used on the *left*, in order to show better the halo evolution, whereas the *right* panels are more appropriate for the disk evolution. In all panels, results for the halo are shown in *dashed curves* and for the disk in *solid curves* (*thick* for [Fe/H]>-1 and *thin* for [Fe/H]<-1)

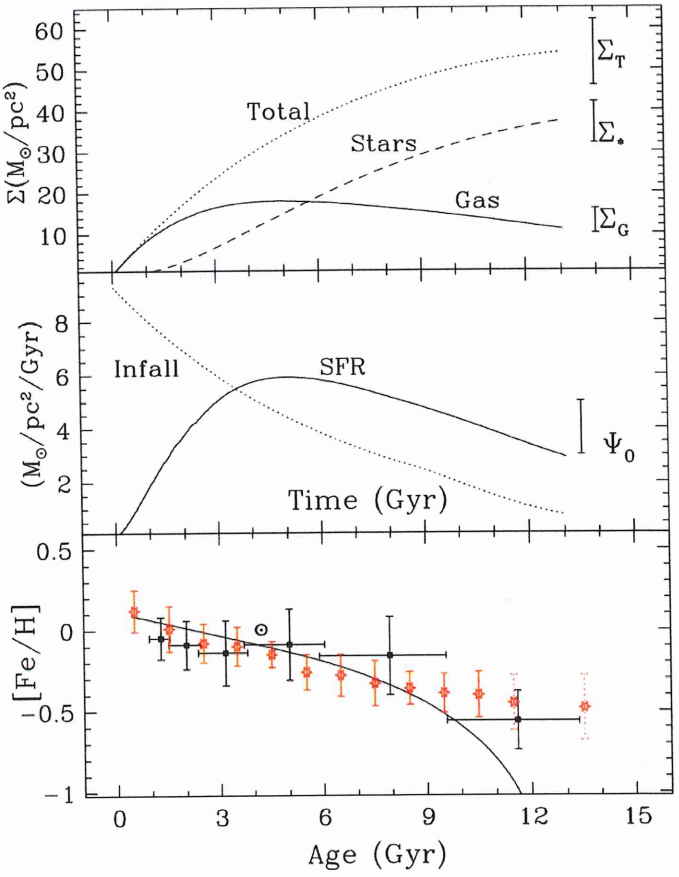

Fig. 5. Comparison of the main observables of the solar neighbourhood to our model predictions. The *upper panel* shows the surface densities of stars, gas and total amount of matter as a function of time. The vertical error bars represent present day values. The *middle panel* shows the star formation rate and infall rate; the current SFR (Ψ_0) is indicated by the error bar. Data for those tow panels are from the compilation of Boissier & Prantzos (1999). In the *lower panel* the solid curve shows the derived age-metallicity relation; data are from Edvardsson et al. (1993, *filled symbols*) and Rocha-Pinto et al. (2000, *open symbols*, with the last two being rather upper limits), while the position of the Sun is shown by the symbol ⊙

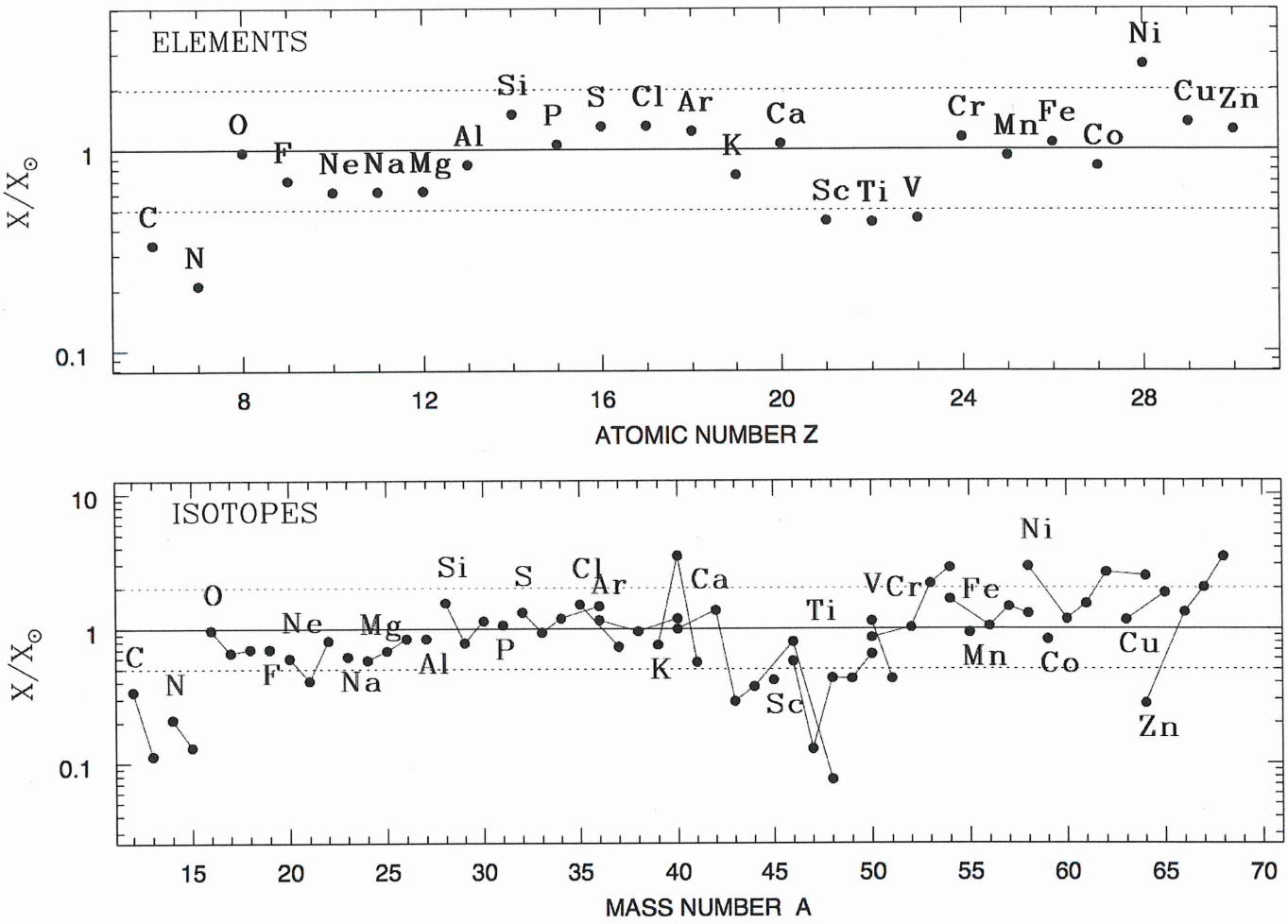

Fig. 6. Ratio of the calculated and observed solar abundances of elements C to Zn (*upper panel*) and their stable isotopes (*lower panel*). Results of our model are shown at a disk age of 8.5 Gyr (Sun's formation), and yields from massive stars (metallicity dependent, from WW1995) and SNIa (from the W7 and W70 models of Iwamoto et al. 1999) are taken into account. The *dotted lines* mark deviations by a factor of 2 from the solar composition. All currently available sets of massive star yields show an underproduction of Sc, Ti and V. C and N also require additional production sources. The overproduction of Ni (in the form of the main isotope ^{58}Ni) results from the W7 model of Iwamoto et al. (1999) for SNIa

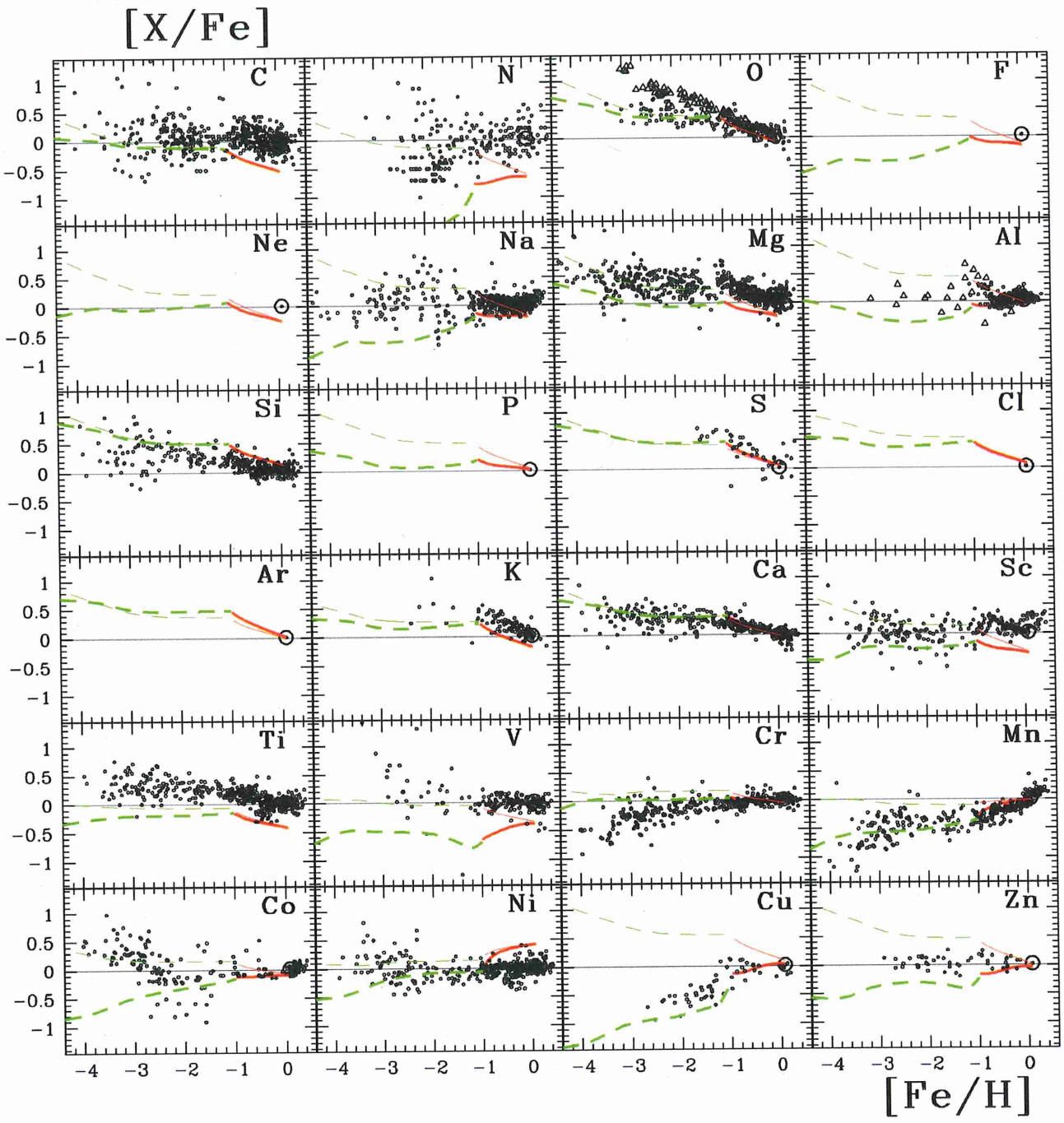

Fig. 7. Abundance ratios [X/Fe] of stars in the halo and the local disk, as a function of [Fe/H]. Theoretical results are obtained with models that treat properly the halo (*dashed curve* assuming *outflow*) and the disk (*solid curve* assuming *slow infall*). Two sets of massive star yields are used, both from WW1995: at constant (=solar) metallicity (*thin curves*, Case A, only for illustration purposes) and at variable metallicity (*thick curves*, the reference Case B). Yields of the W7 and W70 models of Iwamoto et al. (1999) for SNIa are used in both cases (properly interpolated as a function of metallicity); intermediate mass stars are not considered. It should be noted that WW1995 yields of Fe have been divided by 2, in order to obtain the observed α/Fe ratio in halo stars. Model trends below [Fe/H]=-3 are due to the finite lifetime of stars ([Fe/H]=-4 is attained at 10 Myr, corresponding to the lifetime of stars with mass $> 20M_{\odot}$, while [Fe/H]=-3 is attained at 20 Myr, corresponding to the lifetime of $\sim 10M_{\odot}$ stars). In view of the yield uncertainties of individual stars (Sect. 2) and of the uncertainties in the timescales at those early times of the halo evolution, those trends *should not be considered as significant*. The observed data points in the figure are taken from sources listed in Table 1. Observed abundance ratios of [O/Fe] from Israelian et al. (1998) and Boesgaard et al. (1999) are shown by *open triangles*; they suggest a trend quite different from all other alpha-elements. The *open triangles* in the [Al/Fe] panel correspond to observed data with NLTE corrections (from Baumüller & Gehren 1997)

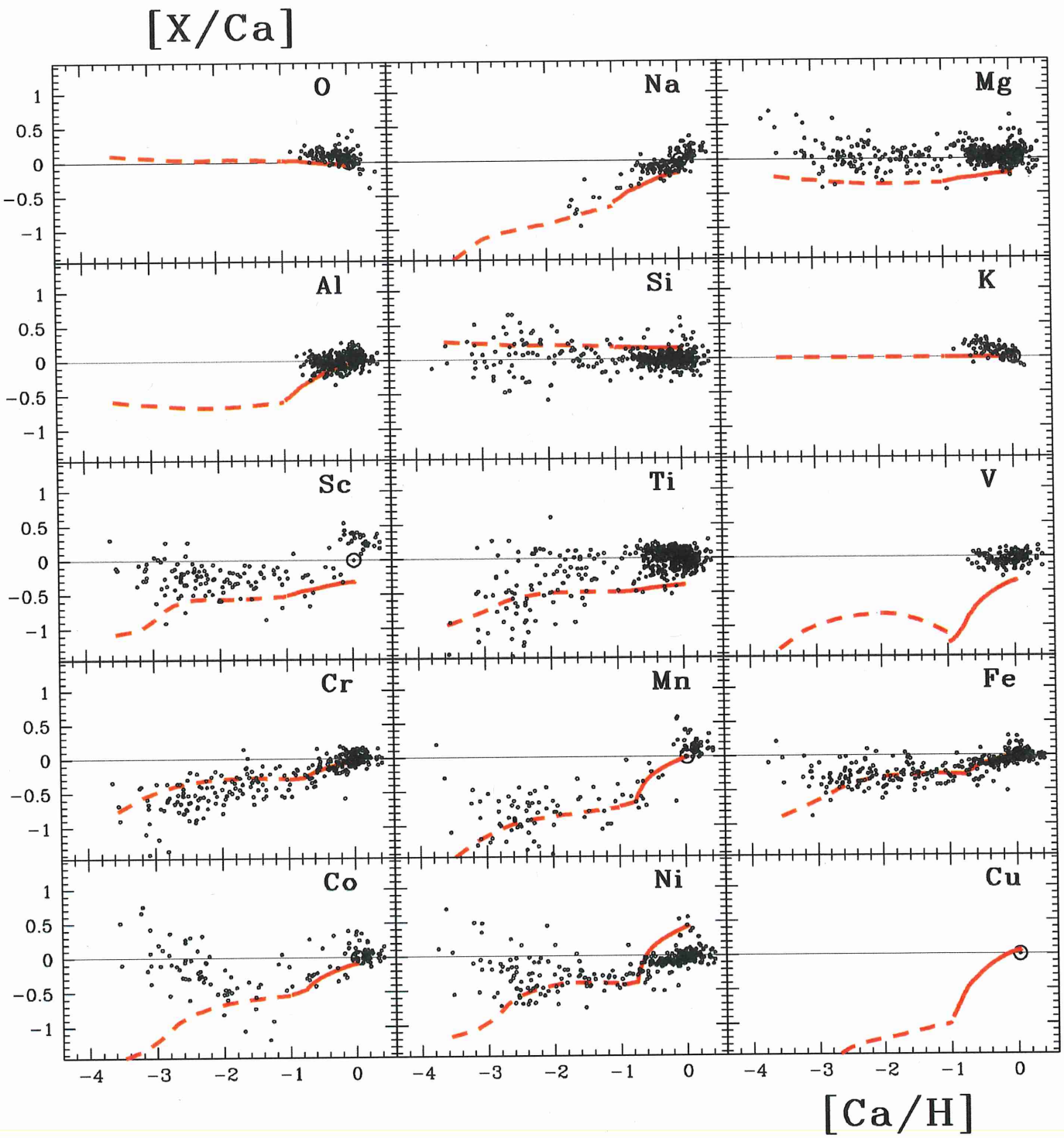

Fig. 8. Evolution of element/Ca abundance ratios as a function of Ca/H. Observations are from references listed in Table 1. Theoretical results (*dashed curves* for the halo and *solid curves* for the local disk) are obtained with the metallicity dependent yields of WW1995 for massive stars and the W7 and W70 models for SNIa (Iwamoto et al. 1999). By adopting Ca as a reference element, some of the uncertainties related to Fe are removed

However, the effect may have been underestimated. After all, stellar mass loss is yet poorly understood. Suppose then that, starting at [Fe/H]∼-3, massive stars produce less and less oxygen as their metallicity increases, because an ever larger part of their envelope is removed. Their inner layers, producing the other α-elements and Fe, are not affected by mass loss; the resulting α/Fe abundance ratio is constant with metallicity, while the corresponding O/Fe is decreasing with metallicity. The

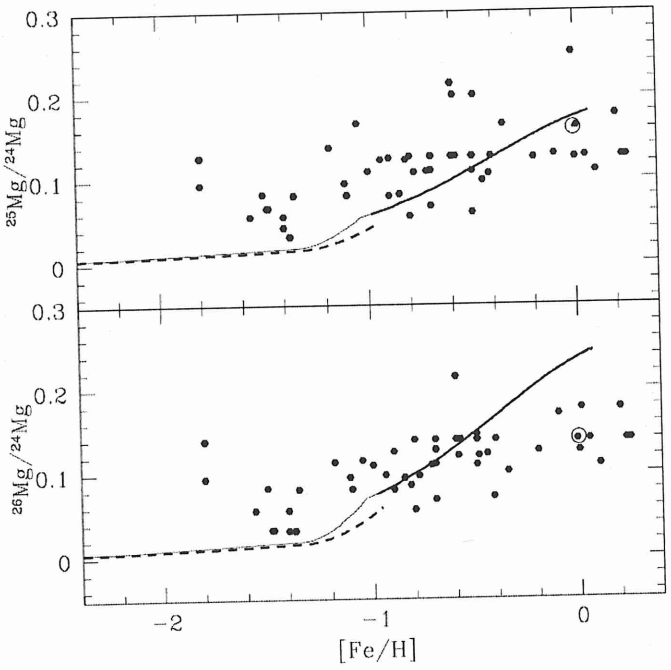

Fig. 10. Evolution of the isotopic abundance ratios of Mg as a function of metallicity [Fe/H]. The *upper panel* shows the evolution of $^{25}Mg/^{24}Mg$ and the *lower panel* the evolution of $^{26}Mg/^{24}Mg$ with respect to [Fe/H]. In both panels the *solid curve* corresponds to the disk model and the *dashed curve* to the halo model. The observed isotopic ratios are from Gay & Lambert (2000), McWilliam & Lambert (1988), Burbuy et al. (1985), Barbuy (1985, 1987), Lambert & McWilliam (1986) and Tomkin & Lambert (1980). Corresponding solar ratios in both panels are shown with ⊙

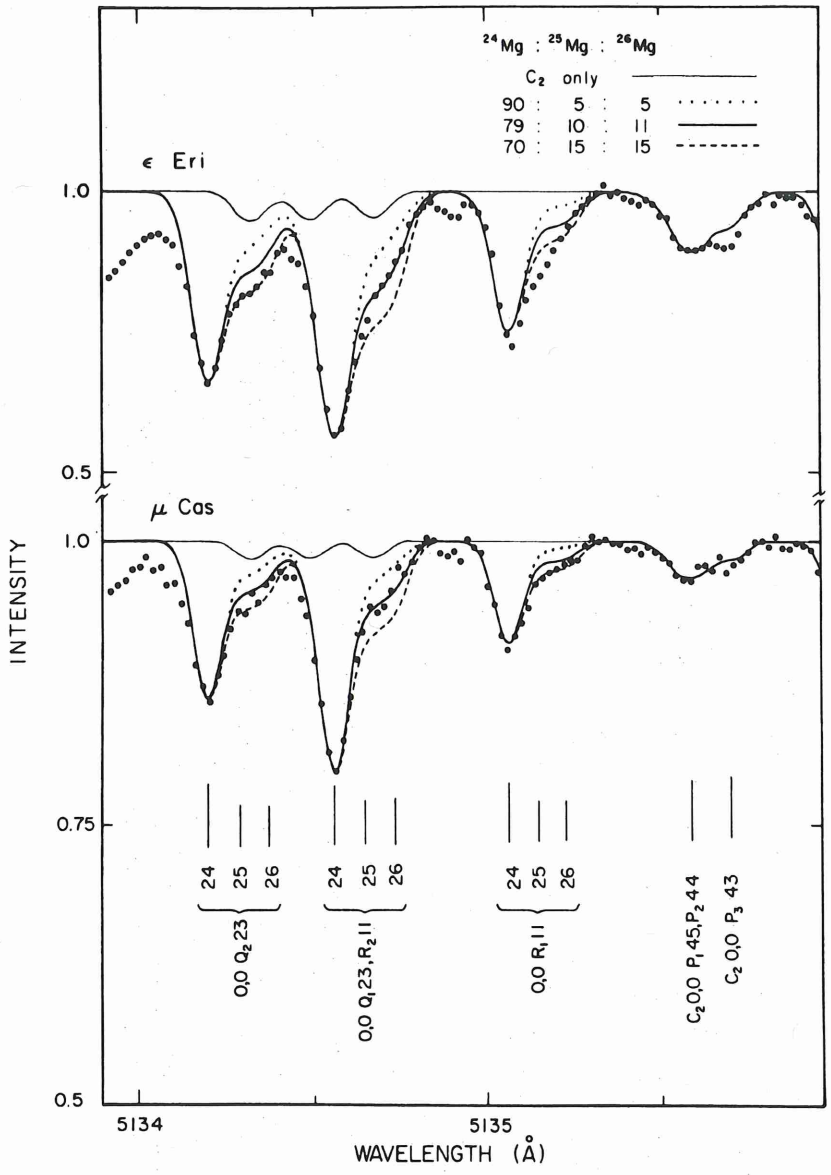

FIG. 1.—Three MgH (0, 0) band lines in ε Eri and μ Cas fitted with synthetic spectra computed for three different Mg isotope mixtures. The synthetic spectrum for C_2 lines alone is also shown. The strength of the C_2 lines is set by matching the strength of the C_2 line at 5135.6 Å.

check of the strength of α-system TiO lines in 61 Cyg B was made with an echelle Reticon spectrum centered at 5285 Å of (0, 0) band α-system lines. The Ti abundance needed for a match of the computed and observed strength of the (0, 0) band lines in this spectrum was in good agreement with the Ti abundance demanded by the (0, 1) and (1, 2) band lines.

In 61 Cyg A, which is hotter than 61 Cyg B, TiO is much weaker than in 61 Cyg B. This weakness has the advantage that it has, at most, a minor effect on the analysis of MgH in 61 Cyg A; however, because of this weakness, it is difficult to make a direct measurement of the strength of α-system TiO lines. An indirect estimate of their strength was made via the much stronger lines of the γ system. (Echelle Reticon spectra, obtained for an investigation of Ti isotopes in late-type stars by Clegg, Lambert, and Bell 1979, were used to make this estimate.)

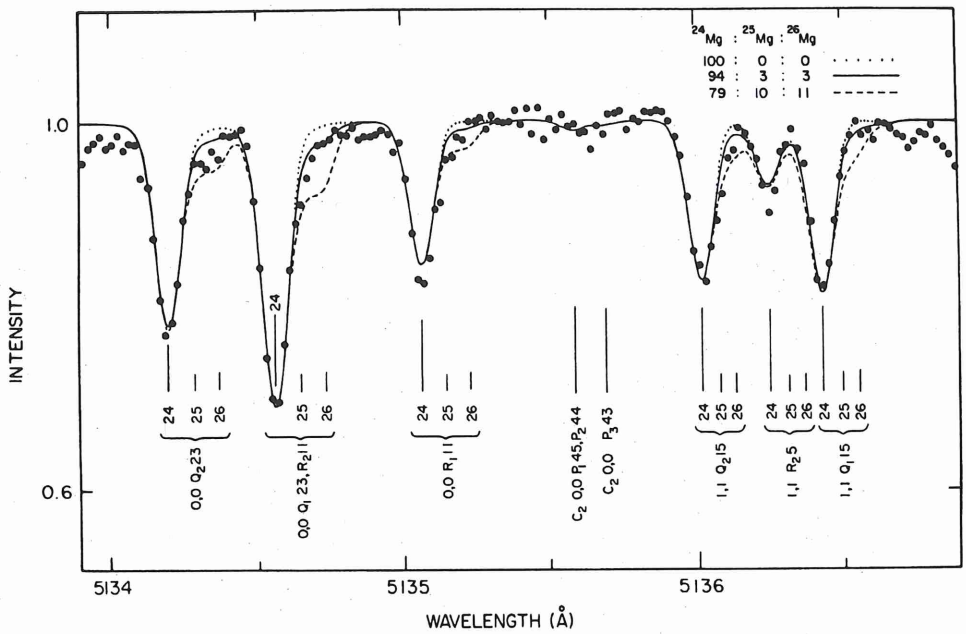

FIG. 2.—MgH (0, 0) and (1, 1) band lines in Gmb 1830 fitted with synthetic spectra computed for three different Mg isotope mixtures. The ^{25}MgH and ^{26}MgH lines are much weaker than in the synthetic spectrum computed with a terrestrial mixture (^{24}Mg:^{25}Mg:^{26}Mg = 79:10:11). The synthetic spectrum computed with ^{24}Mg:^{25}Mg:^{26}Mg = 94:3:3 fits the data best. The C_2 lines are so weak that they have no significant effect on the profiles of the MgH lines.

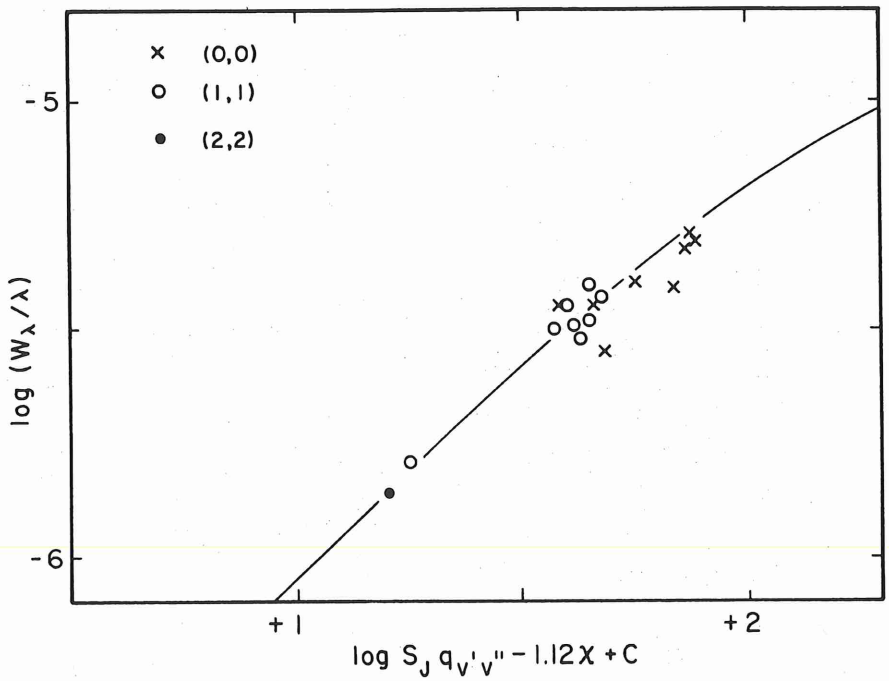

FIG. 3.—MgH curve of growth in Gmb 1830 fitted with a curve of growth computed for MgH and no microturbulence

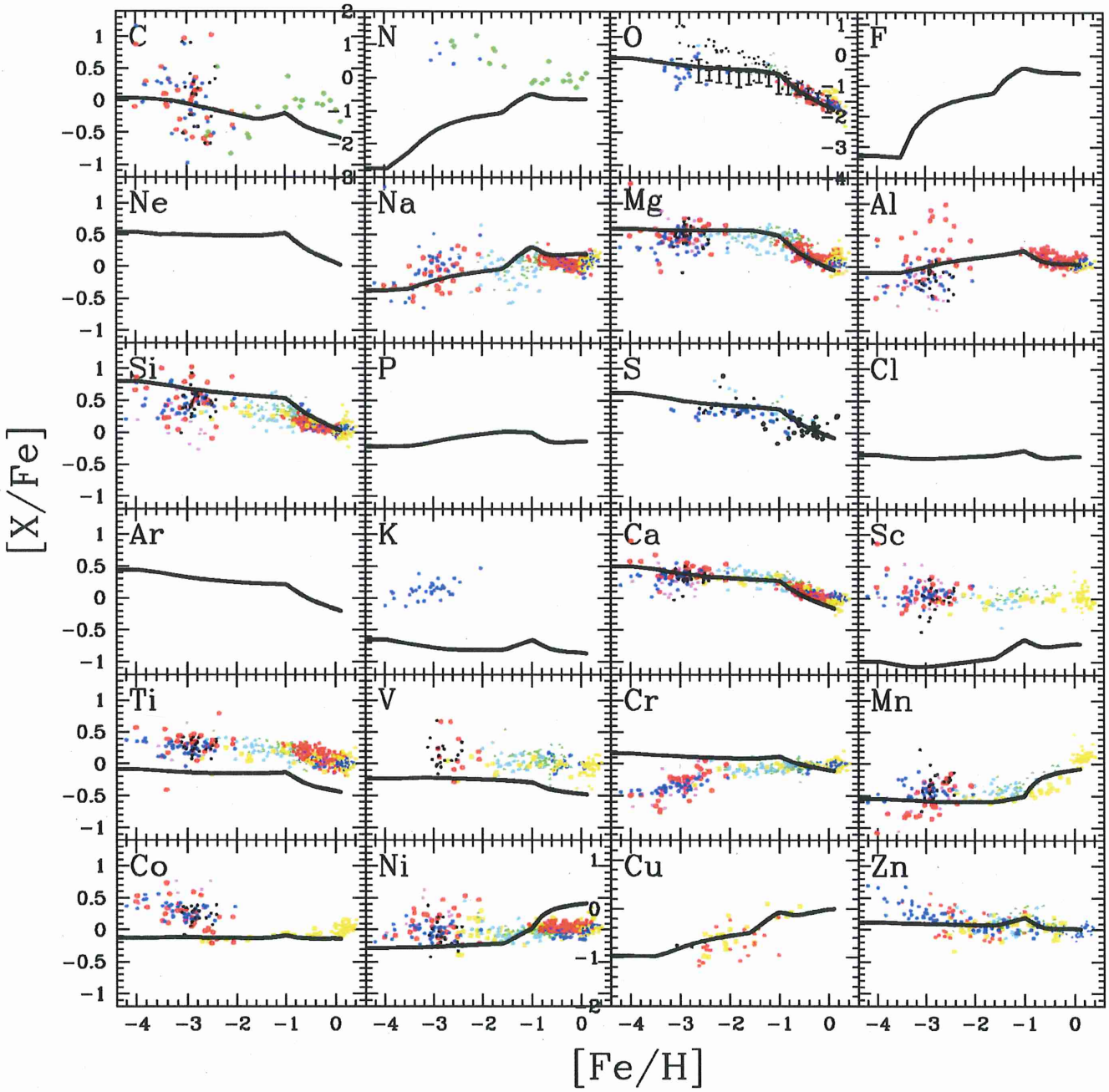
C
N
O
F
Ne
Na
Mg
Al
Si
P
S
Cl
Ar
K
Ca
Sc
Ti
V
Cr
Mn
Co
Ni
Cu
Zn
[X/Fe]
[Fe/H]

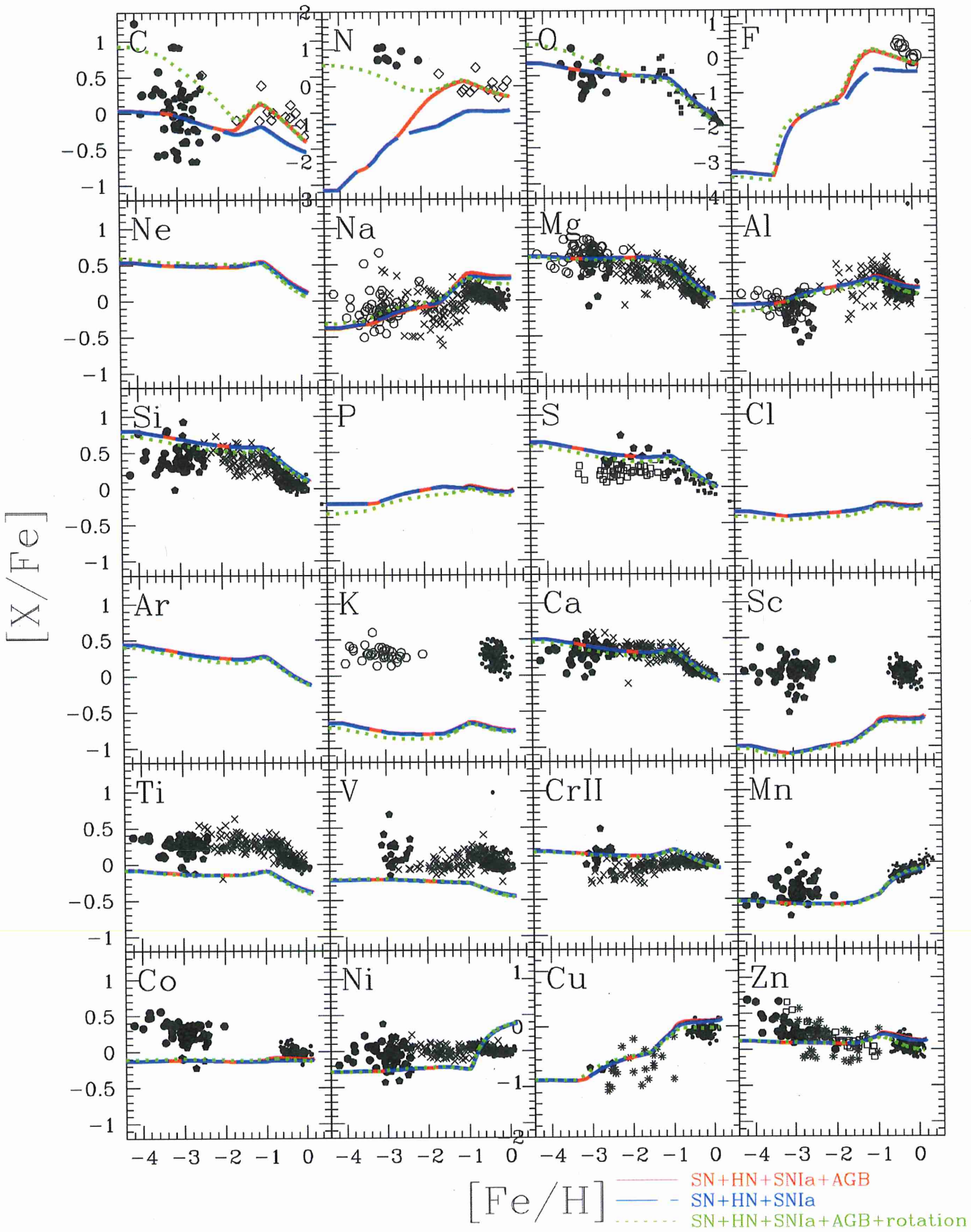

Figure 13. Evolution of elemental abundance ratios [X/Fe] against [Fe/H] for the solar neighbourhood with SNe II, HNe, and SNe Ia only (dashed lines), with AGB stars (solid lines), and with rotating massive stars at $Z = 0$ (dotted lines). The dots are observational data (see KN11 for the references). For C and N, only unevolved stars are plotted.

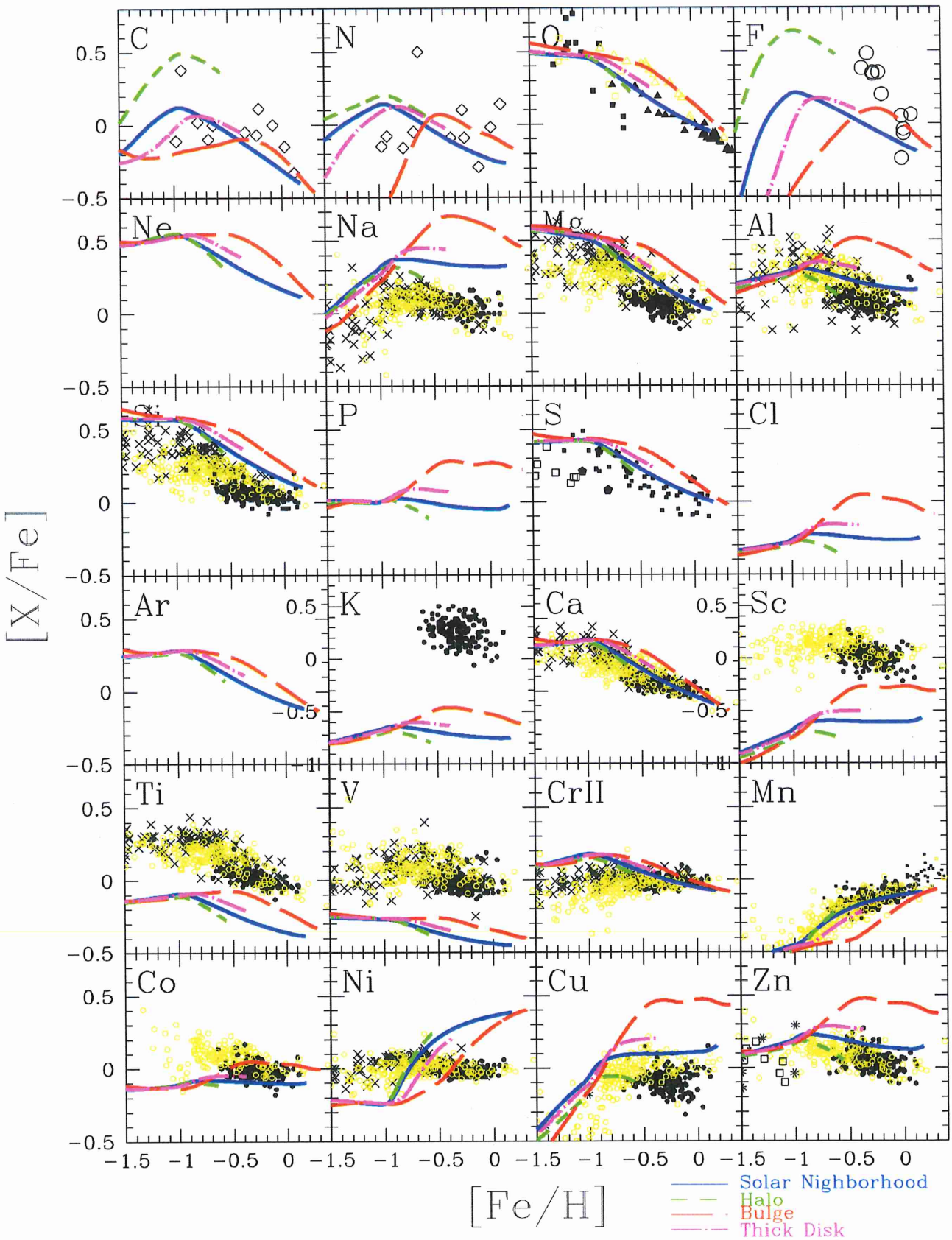

Figure 14. Evolution of elemental abundance ratios [X/Fe] against [Fe/H] for the solar neighbourhood (solid lines), halo (short-dashed lines), bulge (long-dashed lines), and thick disk (dot-dashed lines) with AGB yields. The black and yellow dots are observational data for thin and thick disk stars (see KN11 for the references).

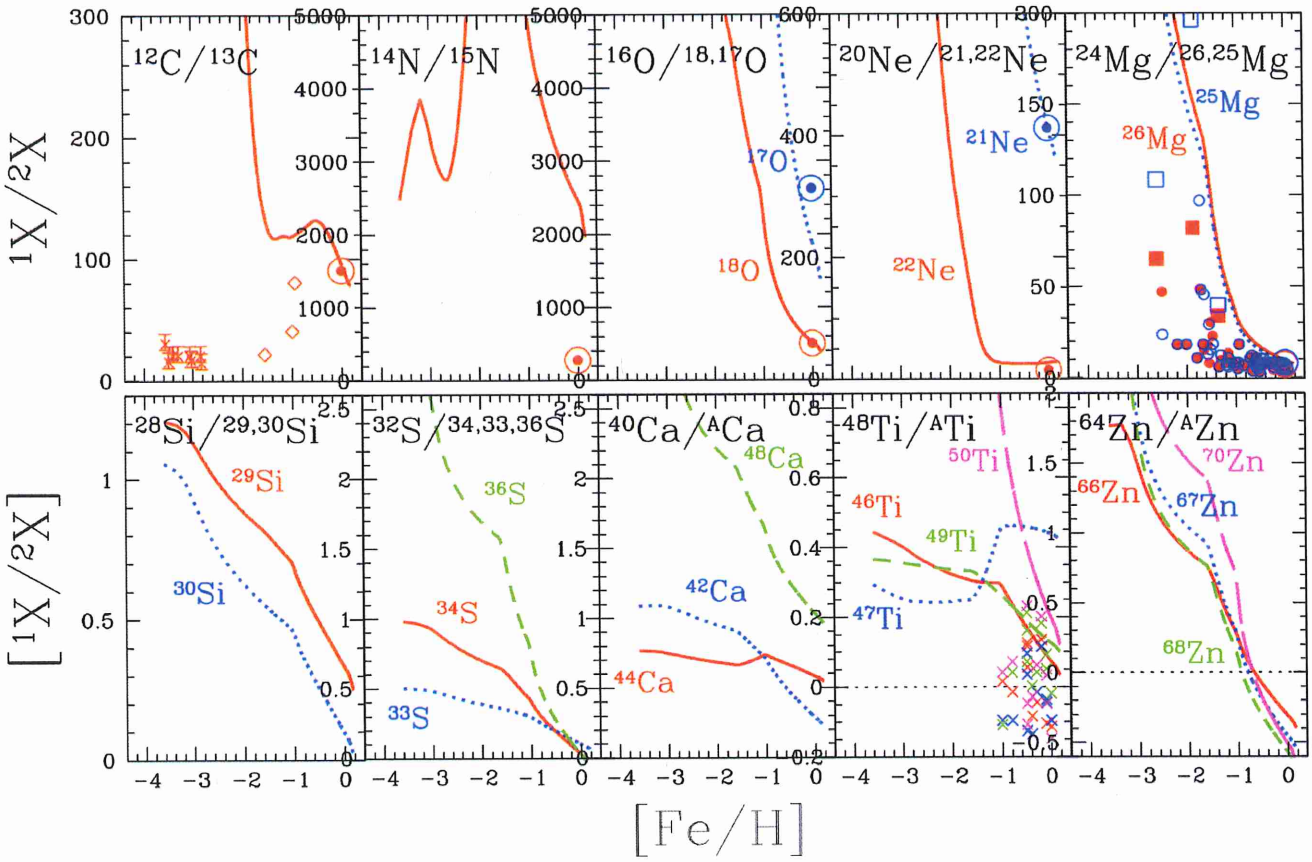

Figure 17. Evolution of isotope ratios against [Fe/H] for the solar neighbourhood (solid lines) with AGB yields. Observational data sources include: For C, Carretta et al. (2000), diamonds; Spite et al. (2006), asterisks; For Mg, Yong, Lambert, & Ivans (2003), open and filled circles for ^{25}Mg and ^{26}Mg; Meléndez & Cohen (2007), open and filled squares for ^{25}Mg and ^{26}Mg; For Ti, Chavez & Lambert (2009), crosses. The solar ratios (Anders & Grevesse 1989) are shown with the solar symbols at [Fe/H] = 0 in the upper panels.

• Carbon — The ^{12}C/^{13}C ratio is $\sim$ 4200 at [Fe/H] = -2.6, and decreases to 109 at [Fe/H] = -1.1 because of the production of ^{13}C from $4-7M_{\odot}$ AGB stars. Then, because of the production of ^{12}C from $1-4M_{\odot}$ AGB stars, the ratio increases until [Fe/H] $\sim$ -0.5, and then decreases to be 88.6 at [Fe/H] = 0, which is consistent with the solar ratio of 89.9 (solar symbol, AG89) and 89.4 (Asplund et al. 2009, hereafter AGSS09). The isotopic fraction of ^{13}C is 0.02%, 0.84%, 0.75%, and 1.03% at [Fe/H] = $-2.6, -1.1, -0.5$ and 0, respectively. The other dots (crosses and diamonds) show the observational data of metal-poor unevolved stars (Carretta et al. 2000; Spite et al. 2006). The low carbon isotopic values of these stars suggests that intermediate-mass AGB stars and/or rotating massive stars have contributed to galactic chemical evolution at a very low metallicity. Note that in the low-mass stellar models, non-standard *extra mixing* processes are not included (e.g. Nollett, Busso, & Wasserburg 2003). These processes may occur during the first and asymptotic giant branches and result in an increase the yields of ^{13}C (and ^{14}N). While the effect of such processes may be minimal on the yields at solar metallicity, they may be substantial for $Z \lesssim 0.0001$, resulting in much smaller predicted ^{12}C/^{13}C ratios from the AGB models than given by the yields of Karakas (2010).

• Nitrogen — Although ^{15}N destruction by AGB stars is neglected in our models, the ^{14}N/^{15}N ratio at [Fe/H] = 0 is still predicted to be larger than the ratio provided by AG89 (272). At [Fe/H] = 0, the isotopic fraction of ^{15}N is 0.04%, which is $6-10$ times smaller than the solar ratio: 0.37% in AG89 and 0.23% in AGSS09. Note that the proto-solar nebula value for the ^{14}N/^{15}N ratio in AGSS09 is 447, a factor of 1.6 higher than the AG89 value. This is because AGSS09 adopt the Jupiter nitrogen isotope value as the proto-solar value, noting that the AG89 ratio is the terrestrial value derived from air and has likely experienced isotopic fractionation and an increase in the abundance of ^{15}N (see Meibom et al. 2007, for more details). That our predicted nitrogen isotope value is too high is probably because the effect of novae, which likely produced a substantial fraction of the ^{15}N in the Galaxy (Romano & Matteucci 2003), are not included in our models. In novae, the accreted hydrogen is heated up to $\sim 2-3\times10^{8}$ K, where the CNO cycle is limited by β-decays rather than the proton capture rate of ^{14}N (the hot CNO burning, Wallace & Woosley 1981). Therefore, ^{13}C, ^{15}N, and ^{17}O are over-produced with respect to

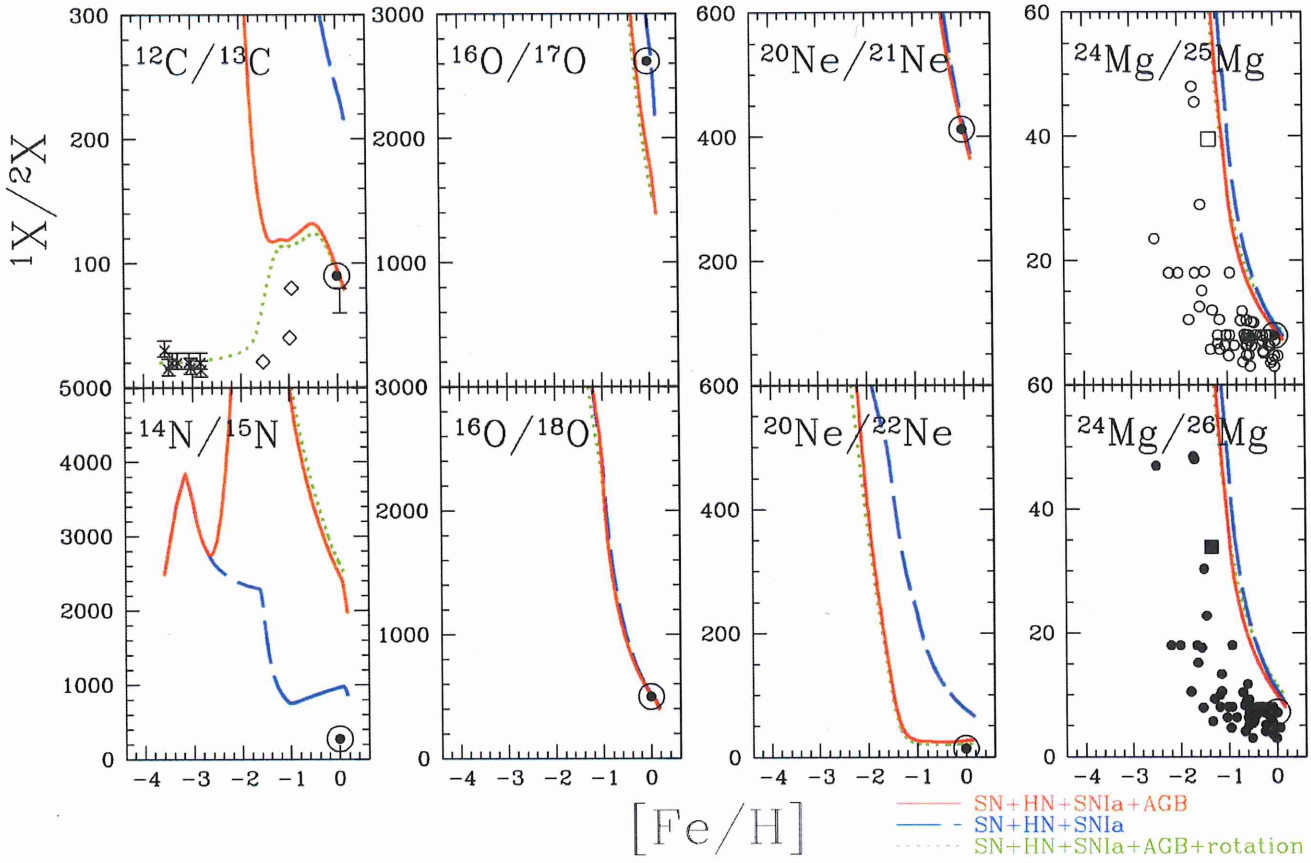

Figure 18. Evolution of isotope ratios against [Fe/H] for the solar neighbourhood with SNe II, HNe, and SNe Ia only (dashed lines), with AGB stars (solid lines), and with rotating massive stars at $Z = 0$ (dotted lines). See Fig.17 for the observational data sources.

the solar abundances. The nucleosynthesis yields depend on the mass of the CO and ONe white dwarfs, and the mixing levels between the accreted envelope and the white dwarfs (José & Hernanz 1998). The rate of novae in the Galaxy is estimated to be about 30 per year (José & Hernanz 1998), but the time evolution of the rate is uncertain.

• Oxygen — Both the $^{16}O/^{17}O$ and $^{16}O/^{18}O$ ratios rapidly decrease from $\sim$ 190000 and $\sim$ 14000 at [Fe/H] $= -2.6$ to 1787 and 457 at [Fe/H] $= 0$ because of the metallicity dependence of massive star nucleosynthesis. The isotopic fractions are (^{16}O:^{17}O:^{18}O) = (99.99, 0.0005, 0.006), (99.96, 0.006, 0.037), (99.87, 0.026, 0.109), and (99.75, 0.053, 0.194) at [Fe/H] $= -2.6, -1.1, -0.5$, and 0, respectively. At [Fe/H]=0, the ^{18}O fraction is consistent but ^{17}O is too large when compared with the solar ratios, (99.76, 0.038, 0.201) in AG89 and (99.76, 0.038, 0.200) in AGSS09. ^{17}O and ^{18}O are mainly produced by $^{16}O(p,\gamma)^{17}F(\beta^+)^{17}O$ in the H-burning layer and $^{14}N(\alpha,\gamma)^{18}F(\beta^+)^{18}O$ in the He-burning layer, respectively, and thus their abundances depend on the amount of the seed element. ^{18}O is mainly produced by He-burning in massive stars and is slightly destroyed in AGB stars. ^{17}O is over produced by AGB stars. The model that adopts only supernova yields (dashed line in Fig. 18) produces a $^{16}O/^{17}O$ ratio that is consistent with the solar ratio. Including the contribution from AGB stars lowers the predicted $^{16}O/^{17}O$ ratio to a value lower than the solar ratio. Note that for the majority of AGB stars in galaxies ($Z \geqslant 0.004$), the ^{17}O yield is increased with the new reaction rates (§2). The oxygen isotopic ratios may be used to put constraints on the rates of the $^{17}O(p,\alpha)^{14}N$ and $^{17}O(p,\gamma)^{18}F$ reactions in AGB nucleosynthesis models. Novae also produce some ^{17}O (and ^{13}C), which would worsen the situation.

• Neon — The $^{20}Ne/^{21}Ne$ and $^{20}Ne/^{22}Ne$ ratios show a similar decrease as oxygen. With AGB yields, the isotopic fractions at [Fe/H]$= 0$ are consistent with the solar ratio: (^{20}Ne:^{21}Ne:^{22}Ne) = (96.16, 0.23, 3.61) in the model, (92.99, 0.23, 6.78) in AG89, and (92.94, 0.22, 6.83) in AGSS09. The only data for comparison is meteoritic.

• Magnesium — The $^{24}Mg/^{25}Mg$ and $^{24}Mg/^{26}Mg$ ratios also show a rapid decrease from 247 and 271 at [Fe/H] $= -2.6$ to 8.54 and 9.22 at [Fe/H] $= 0$ because the production of the minor isotopes increases in metal-rich supernovae. The $^{24}Mg/^{25}Mg$ and $^{24}Mg/^{26}Mg$ ratios are a bit larger than the observations of stars (dots, Yong, Lambert, & Ivans 2003; Meléndez & Cohen 2007) and the solar ratios (7.92 and 7.19 in AG89), which suggests that AGB stars (or Wolf-Rayet stars) need to contribute more at all metallicities. The isotopic fractions are (^{24}Mg:^{25}Mg:^{26}Mg) = (99.28, 0.39, 0.34), (95.60, 2.30, 2.11), (88.09, 5.77, 5.13), and (82.46, 9.28, 8.26) at [Fe/H] $= -2.6, -1.1, -0.5$, and

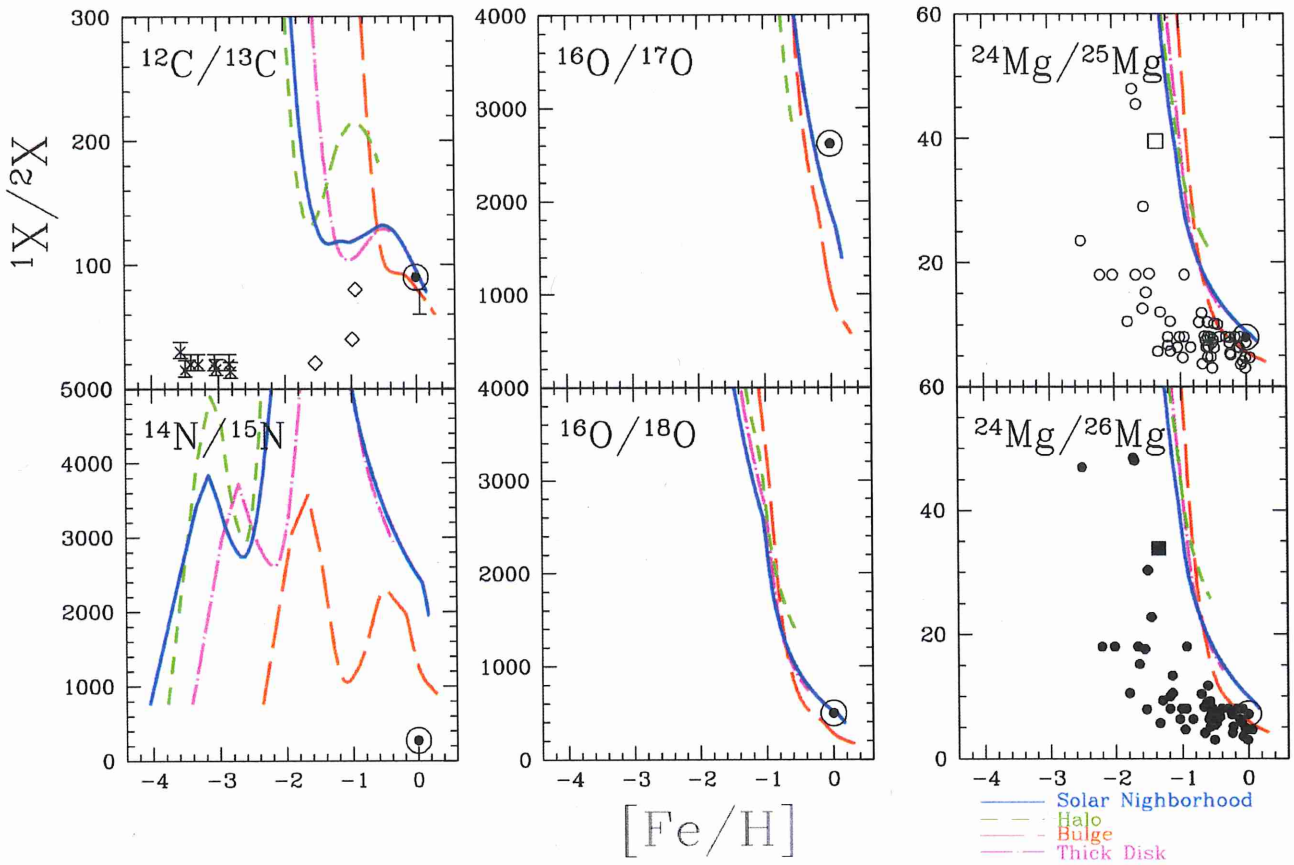

Figure 19. Evolution of isotope ratios against [Fe/H] for the solar neighbourhood (solid lines), halo (short-dashed lines), bulge (long-dashed lines), and thick disk (dot-dashed lines) with AGB yields. See Fig.17 for the observational data sources.

0, respectively. The isotopic fractions of solar ratios are (79.03, 9.97, 10.99) in AG89 and (78.99, 10.00, 11.01) in AGSS09. In both observations, ^{26}Mg is more abundant than ^{25}Mg, which is the opposite both for the AGB stars and supernovae yields. In supernovae, there is a metallicity dependence on the predicted Mg isotopic ratios. ^{24}Mg is mainly produced by the reaction ^{12}C+^{12}C and is a primary isotope. On the other hand, ^{25}Mg and ^{26}Mg are secondary isotopes and are significantly produced by higher metallicity stars. They are mainly produced by the following reactions: ^{24}Mg$(p,\gamma)^{25}$Al$(\beta^+)^{25}$Mg$(p,\gamma)^{26}$Al$(\beta^+)^{26}$Mg and thus their abundances depend on the amount of the seed element, ^{24}Mg. In AGB stars, there is no such metallicity dependence. The neutron-rich Mg isotopes are produced by α-captures onto ^{22}Ne via ^{22}Ne$(\alpha,n)^{25}$Mg and ^{22}Ne$(\alpha,\gamma)^{26}$Mg (Karakas & Lattanzio 2003). The AGB yields of the neutron-rich Mg isotopes depends on the amount of ^{22}Ne in the He-burning region, and this can have a primary component in intermediate-mass AGB stars, where the ^{22}Ne is produced from primary nitrogen made by HBB.

- Si, S, Ca, Ti, and Zn — For heavier elements most of the ratios at [Fe/H] = 0 are roughly consistent with the solar ratios, but the predictions for ^{29}Si, ^{48}Ca, ^{47}Ti are smaller than the solar ratios. These may require the update of the mixing treatment and reaction rates in the supernovae calculations. For Zn, the offsets from the solar ratios are possibly caused by the under-production of ^{64}Zn. Although neutron-rich isotopes of Zn could be produced by neutron-capture processes, ^{64}Zn is mostly produced by the higher energy and entropy experienced during supernova explosions. In fact, if we were to set a higher fraction of hypernovae, the isotopic ratios become closer to the solar ratios.

The model dependence on the evolution of the isotope ratios is shown in Figure 18. With the contribution from AGB stars (solid lines), the ^{12}C/^{13}C and ^{20}Ne/^{22}Ne ratios become consistent with the solar ratio, and ^{24}Mg/^{25,26}Mg becomes slightly closer to the observations. However, as mentioned above, the ^{16}O/^{17}O ratio is consistent with the model without an AGB contribution (dashed lines). This is different from Timmes, Woosley, & Weaver (1995)'s results, where the ^{16}O/^{17}O ratio was consistent with the solar ratio without AGB yields and ^{18}O is over-produced by supernovae. This is due to our use of updated supernova yields. For heavier elements, there is only a $\sim$ 0.01 dex difference around [Fe/H] $\sim$ 0 for the models with and without AGB yields. For ^{24}Mg/^{25,26}Mg, the contribution of AGB stars are larger in Fenner et al. (2003) than in our models, which may be due to differences in the adopted IMF (§2.3).

ISSUES & GAPS

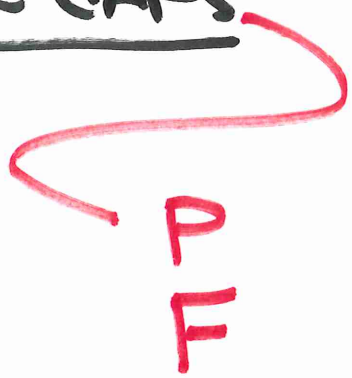

PI — exc. lines ~10555Å (7.0eV)
— UV (HST) lines (1.4eV)

F via HF in IR V-R tpwR
(FI x exc. v. pec. ks) (TEXES)

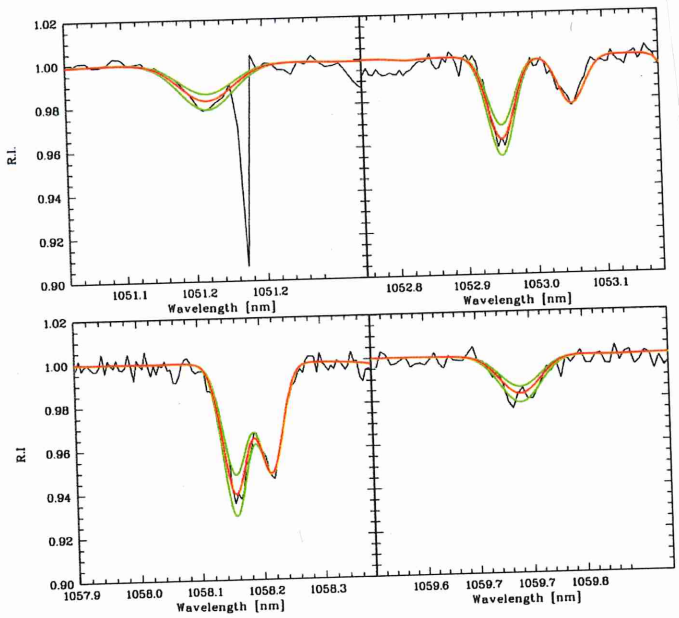

Fig. 1. The four P I lines are here shown in the case of HD 13555. The observed spectrum (solid black) is compared to the synthetic profile (solid red) with the P abundance derived from the *EW* measurement. Also shown are the synthetic profiles obtained by changing the P abundance by ±0.1 dex (solid green). The telluric absorption affecting the 1051 pm line is clearly visible in the upper-left panel.

Caffau et al. 2011 A&A 532 A98

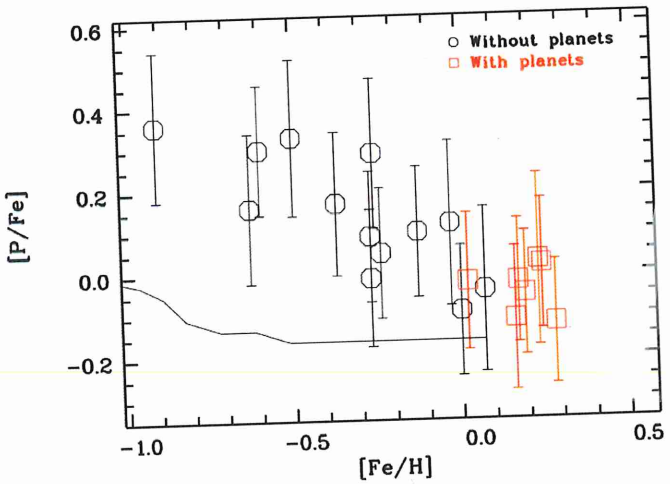

Fig. 2. [P/Fe] as a function of the metallicity, [Fe/H]. The dimension of the symbols reflects the average line-to-line scatter of 0.045 dex. The error bars are the sum under quadrature of the uncertainties of P (the linear sum of line-to-line scatter and the systematic uncertainty) and of Fe, the latter assumed to be 0.1 dex for all stars. Stars known to have planets (red squares) have different symbols from stars without known planet (black hexagons). A model of Galactic evolution of P (Kobayashi et al. 2006) is added (solid line) for comparison to the observed data.

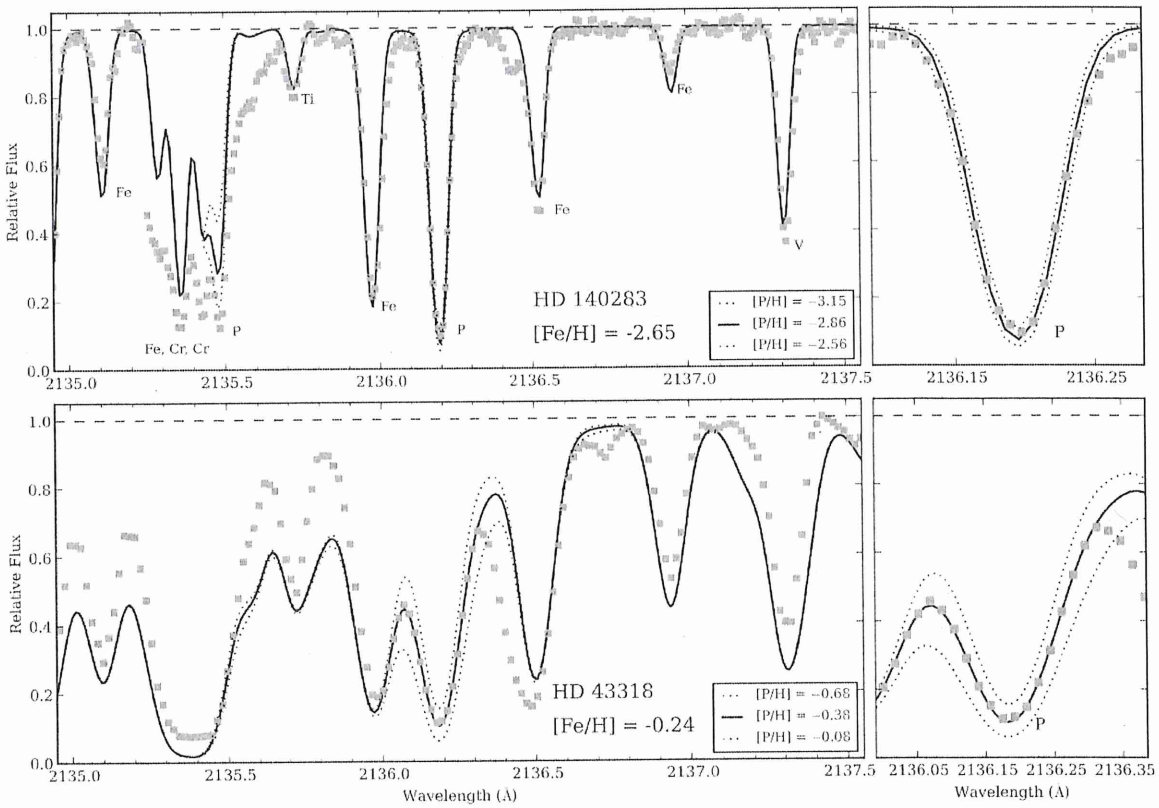

Figure 1. P I 2136 Å region in the STIS spectra of HD 140283 (spectral resolution $R = (\lambda/\Delta\lambda) = 110{,}000$) and HD 43318 ($R = 30{,}000$). The data are represented by gray squares. Absorption features are identified in the top panels. Synthetic spectra of different P abundances are plotted over each spectrum, with the best fit indicated by a bold line. A zoom-in on the 2136 Å line is shown in the right panels. Note that the P abundances shown here include the empirical 0.23 dex correction described in the text.

Jacobson et al. 2014 ApJ 796 24
Roederer et al. 2014 ApJ 797 69

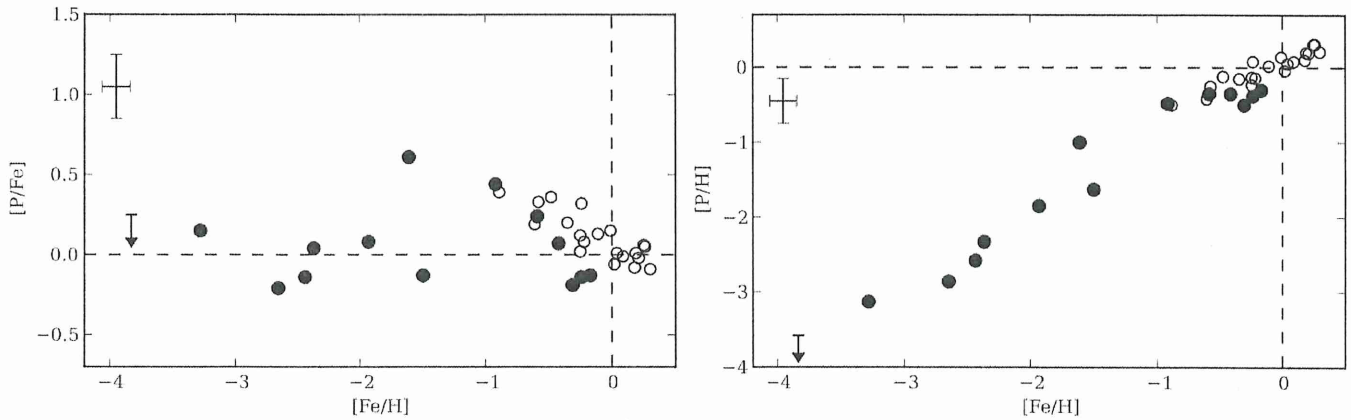

Figure 2. [P/Fe] and [P/H] vs. [Fe/H] for the current study (filled circles and upper limit symbol) along with the sample of Caffau et al. (2011; open circles). A representative error bar for an individual star is given in the top left corner of each panel.

Table 1
Stellar P and Fe Abundances

Star	[Fe/H][a]	σ	[P/H]	σ	[P/Fe]	σ
BD +44 493	−3.83[b]	0.19	< −3.58	...	< +0.25	...
G 64−12	−3.28	0.09	−3.13	0.34	+0.15	0.26
HD 2454	−0.42	0.12	−0.35	0.27	+0.07	0.21
HD 16220	−0.31	0.11	−0.50	0.26	−0.19	0.20
HD 43318	−0.24	0.11	−0.38	0.26	−0.14	0.20
HD 76932	−0.92	0.12	−0.48	0.29	+0.44	0.20
HD 94028	−1.61	0.13	−1.00	0.29	+0.61	0.21
HD 107113	−0.59	0.11	−0.35	0.26	+0.24	0.20
HD 108317	−2.44	0.11	−2.58	0.35	−0.14	0.20
HD 128279	−2.37	0.12	−2.33	0.36	+0.04	0.22
HD 140283	−2.65	0.08	−2.86	0.30	−0.21	0.19
HD 155646	−0.17	0.07	−0.30	0.25	−0.14	0.19
HD 160617	−1.93	0.08	−1.85	0.27	+0.07	0.17
HD 211998	−1.50	0.11	−1.63	0.33	−0.13	0.21

Notes.
[a] These values were determined from the optical spectra.
[b] From Ito et al. (2013).

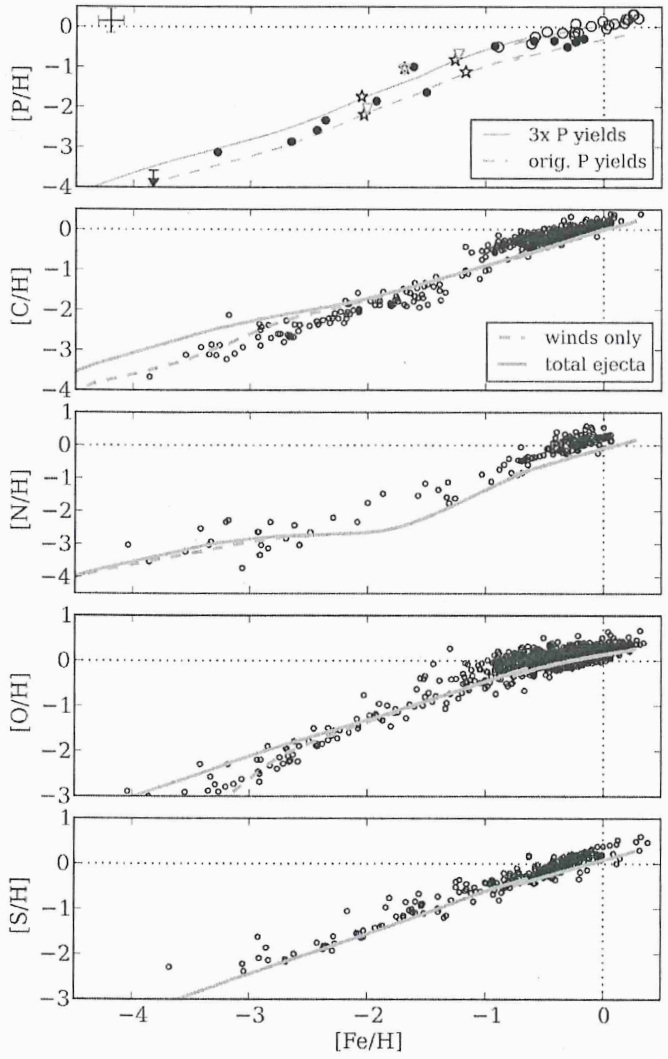

Figure 3. Top panel: stellar [P/H] vs. [Fe/H] as in Figure 2, with the addition of DLA measures (stars) and DLA upper limits (triangles). Also shown are the chemical evolution model of Cescutti et al. (2012), with massive-star P yields from Kobayashi et al. (2006; dashed line) and the yields increased by a factor of three (solid line). These correspond to "Model 6" and "Model 8" in Cescutti et al. (2012), respectively. Remaining panels: the same for elements C, N, O, and S, with stellar abundances taken from the literature. Also in each panel is the prediction for the chemical evolution model for each element. For C, N, and O, two models are shown, the only difference being the treatment of yields from massive stars with $Z < 10^{-5}$ (spin stars). The solid lines indicate total C, N, O ejecta (winds plus supernovae (SNe)), while the dashed lines represent element production in spin star winds only; see Cescutti & Chiappini (2010) for details. References for the literature stellar samples shown here are Israelian et al. (2004), Ramírez et al. (2013), Nissen et al. (2004, 2007), Caffau et al. (2005), Spite et al. (2005, 2011), Lai et al. (2008), Takada-Hidai et al. (2002), Carbon et al. (1987), Reddy et al. (2003, 2006), Fabbian et al. (2009), Shi et al. (2002), Takeda & Takada-Hidai (2011), Ryde & Lambert (2004), Hansen et al. (2011), and Israelian & Rebolo (2001).

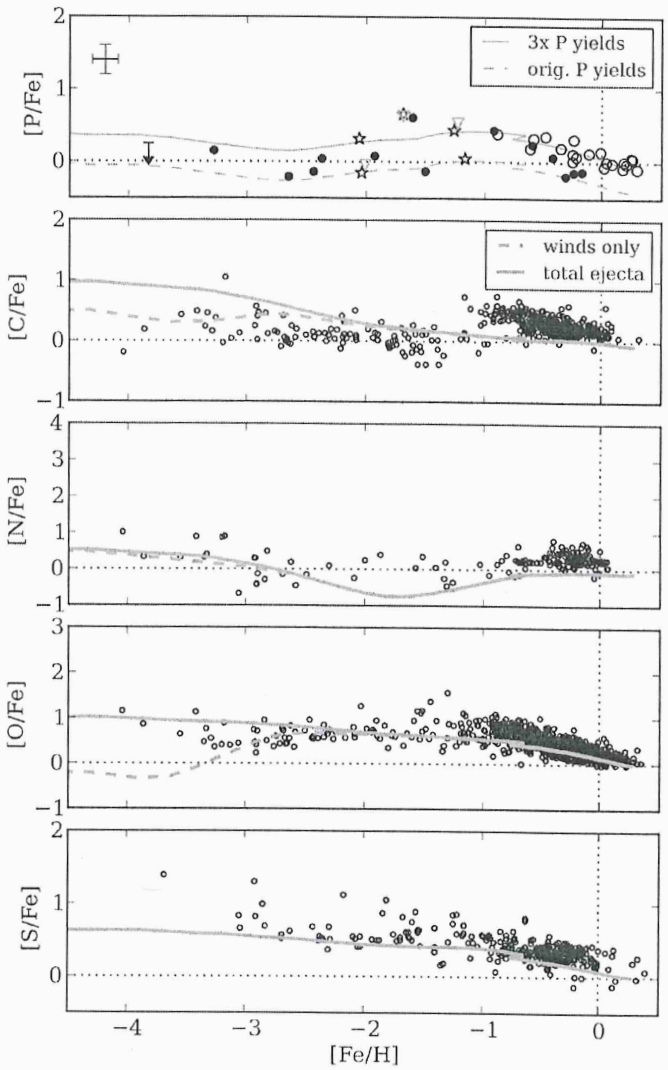

Figure 4. [X/Fe] vs. [Fe/H] for elements P, C, N, O, and S. Symbols and models are the same as in Figure 3.

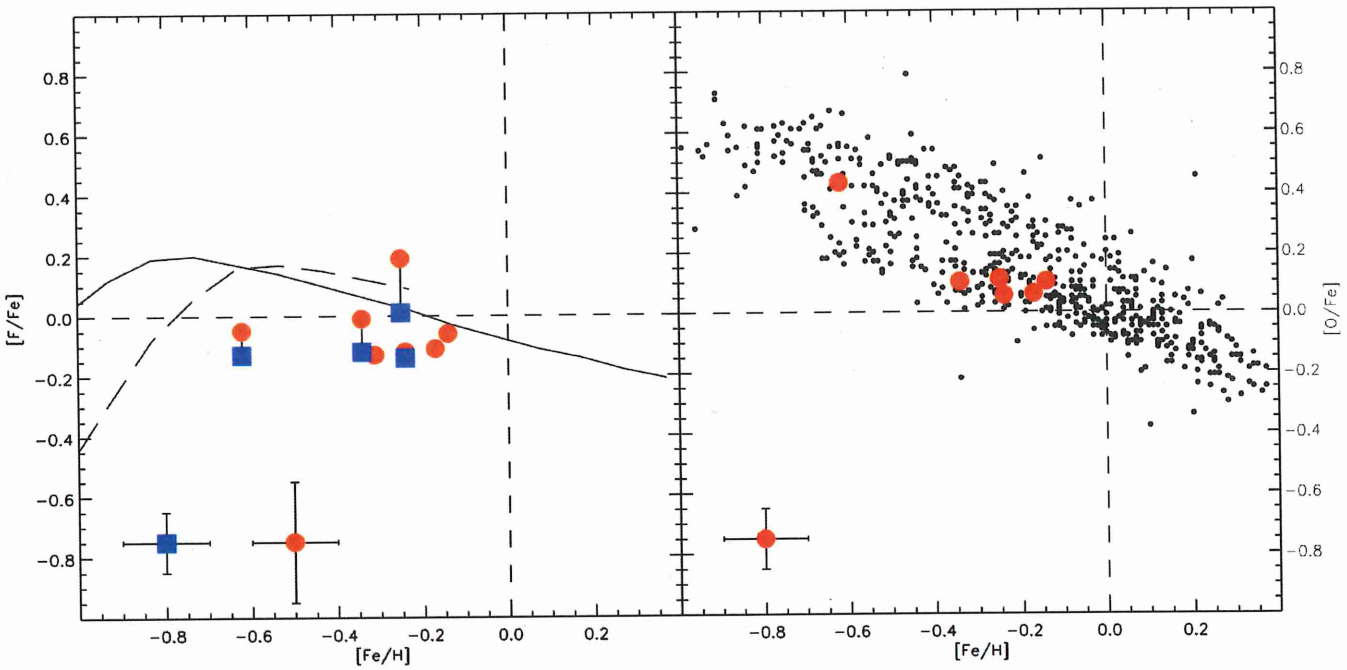

Figure 2. [F/Fe] and [O/Fe] as functions of [Fe/H] for our program stars. Left panel: results from the 2.3 μm HF line are marked with blue squares and results from the 12.2 μm line are marked with red dots. Results for the same stars are interlinked with lines. Also shown are the predictions of the models from Kobayashi et al. (2011b) not including fluorine production in W-R stars or via the ν process. The full line is the solar neighborhood model and the dashed line is the thick disk model. The model predictions have been transformed to the solar abundance scale of $A(F)_{\odot} = 4.40$ (Maiorca et al. 2014) and $A(Fe)_{\odot} = 7.50$ (Asplund et al. 2009). Right panel: the oxygen abundances plotted are the mean of the abundances derived from the 6300 Å [O I] line and 1.55 μm OH lines. The black dots are the solar neighborhood dwarfs of Bensby et al. (2014) consisting of thin- and thick-disk-type stars showing the typical bimodality of lower and higher oxygen enhancement, respectively. Conservative estimates of the uncertainties are marked in the lower left corners in both panels.

(A color version of this figure is available in the online journal.)

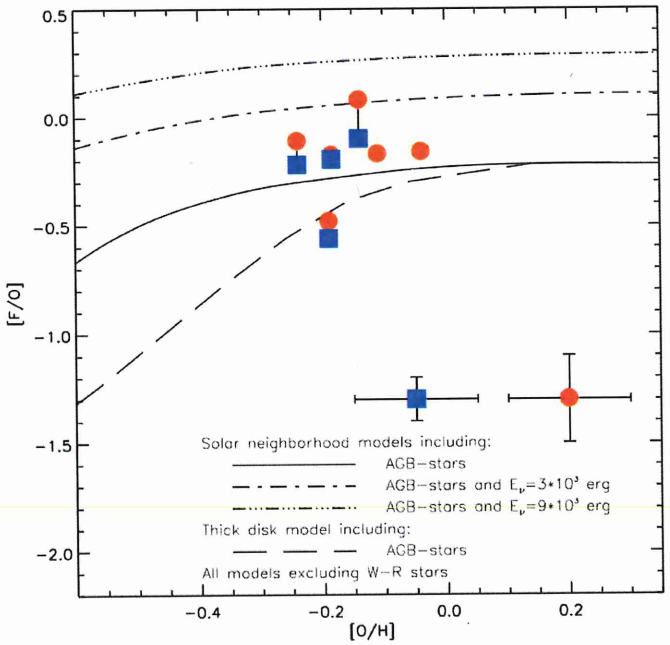

Figure 3. Our fluorine abundances compared with the predictions of the models from Kobayashi et al. (2011a, 2011b). The model predictions have been transformed to the solar abundance scale of $A(F)_{\odot} = 4.40$ (Maiorca et al. 2014) and $A(O)_{\odot} = 8.69$ (Asplund et al. 2009). Results from the 2.3 μm HF line are marked with blue squares and results from the 12.2 μm line are marked with red dots. Results for the same stars are interlinked with lines. Conservative estimates of the uncertainties are marked above the text in the plot.

(A color version of this figure is available in the online journal.)

stars except αTau where the latter value is ~0.2 dex higher than the former. However, because of the strong microturbulence dependence of the 12.2 μm line, this is within the uncertainties. We note that changing the IR microturbulence, within the uncertainty, to 2.5 km s^{-1} will shift this value into the trends of the others in the plots.

Since the fluorine abundances derived from the 2.3 μm and the 12.2 μm lines agree so well using standard MARCS atmospheres for these red giants, we can conclude that the formation of the 12 μm lines are also well described by such models. On the contrary, numerous water lines in this wavelength region are poorly modeled. Ryde et al. (2002, 2006) thus constructed a semi-empirical model atmosphere that could explain the formation of strong water lines. A cooling of the outer atmosphere of a few 100 K, at $\log \tau_{500} < -4$, was needed. This extra outer cooling does not, however, significantly affect the 12.2 μm HF line, since it is formed deeper in the photosphere: the derived fluorine abundance is only 0.07 dex higher for αBoo when using a standard MARCS model compared with using the modified MARCS model of Ryde et al. (2002).

Available chemical evolution models of fluorine in the solar neighborhood predict very similar abundance trends. In Figures 2 and 3 we have chosen to compare our results with the chemical evolution models of Kobayashi et al. (2011b) since, to our knowledge, those are the only models showing the evolution of fluorine from production in only AGB stars. For example, the models of Renda et al. (2004) have chemical evolution of fluorine including (1) the ν process; (2) the ν process and W-R stars; and (3) the ν process, W-R stars, and AGB stars. Since AGB stars are the only source of fluorine that has been observationally proven (see Section 1), we find the combinations of chemical

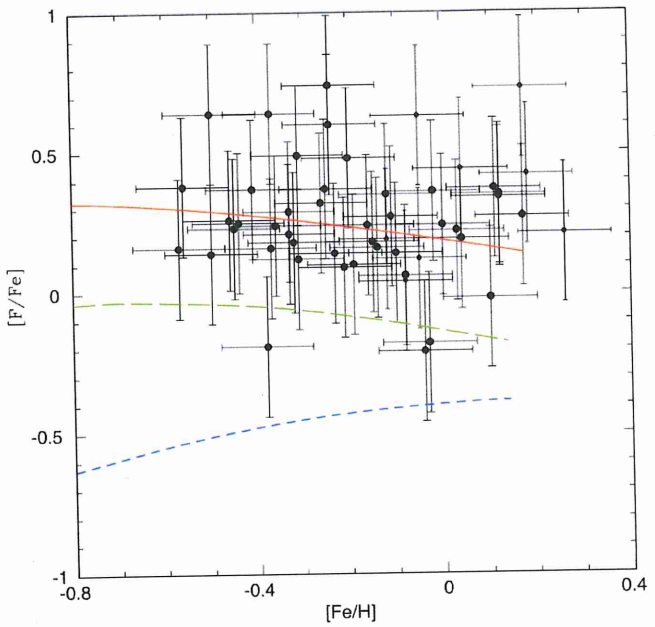

Figure 5. [F/Fe] vs. [Fe/H] for thin disk stars. Chemical evolution models from Kobayashi et al. (2011) are shown for AGB production (small-dashed blue curve), SN plus AGB production (large-dashed green curve), and SN production with neutrino spallation plus contributions from AGB stars (solid red curve).

Pilachowski + Pace
2015 AJ 150 66

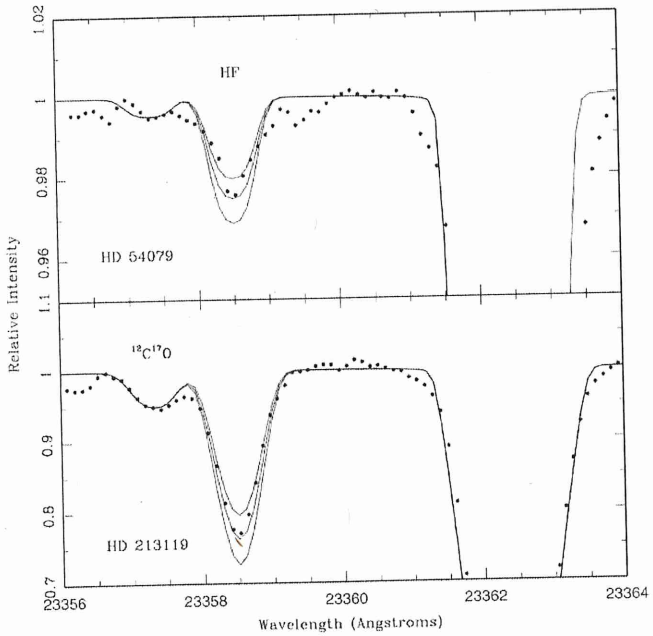

Figure 1. HF spectra of two thin disk stars are shown together with calculated synthetic spectra. The upper panel is the spectrum of HD 54079, a giant with a temperature of 4450 K and [Fe/H] = –0.45. It is shown with synthetic spectra for log A(F) = 3.98, 4.08. and 4.08. The lower panel is the spectrum of HD23119, a giant with a temperature of 4090 K and [Fe/H] = –0.50. It is shown with synthetic spectra for log A(F) = 4.24, 4.34, and 4.44. The $^{12}C/^{17}O$ feature adjacent to HF has been noted in the lower panel.

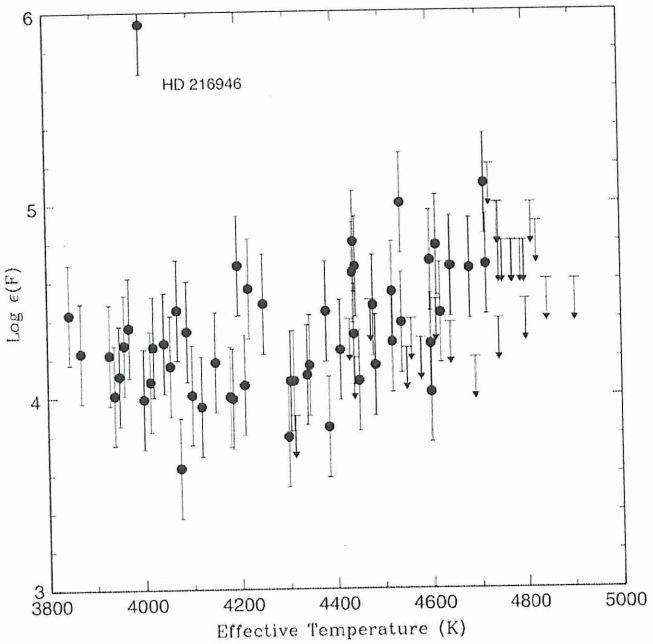

Figure 2. Derived abundance of log ϵ(F) vs. effective temperature. The HF feature becomes undetectable at temperatures above 4700 K. For temperatures $4500 < T_{\rm eff} < 4700$, HF is detectable only if the abundance is high. The M0Iab supergiant HD 216946 (HR 8726) is labeled.

integration on the IMF). Therefore, the contribution from AGB stars (solid lines) is seen at [Fe/H] ~ -2.5. At [Fe/H] ~ -1, [N/Fe] reaches 0.15, which is 0.8 dex larger than the case without AGB yields (dashed lines). At [Fe/H] $\gtrsim -1$, [N/Fe] shows a shallow decrease due to SNe Ia. No difference is seen at [Fe/H] $\lesssim -2.5$ with and without the AGB yields, while [N/Fe] can be as large as ~ 0.5 with rotating massive stars (dotted lines). Chiappini et al. (2006) showed that the contribution from rotating massive stars is required to solve the primary N problem. As noted above, however, AGB stars can also contribute to N production even at [Fe/H] $\lesssim -2.5$ when taking inhomogeneous chemical enrichment into account (KN11). From the difference between C and N, it is possible to distinguish the contribution from low- and intermediate-mass AGB stars as the enrichment source of the observed metal-poor stars. Pols et al. (2009) showed that the IMF with the Gaussian distribution peaked at $\sim 10 M_\odot$ (Komiya et al. 2007) is rejected when trying to match the fraction between C-rich and N-rich stars, based on binary population synthesis models (see also Izzard et al. 2009).

- Fluorine — F is one of the most interesting elements, although F abundances are estimated from only one infrared line from stellar spectra. AGB stars and massive stars have both been suggested to produce F but production has only been confirmed for AGB stars (Jorissen, Smith, & Lambert 1992; Abia et al. 2010). The AGB mass range that produces F is similar for C and is $2 - 4 M_\odot$. Thus the difference is seen only at [Fe/H] $\gtrsim -1.5$. At [Fe/H] ~ -1, [F/Fe] reaches 0.22 in the model with the AGB yields (solid lines). This is 0.56 dex larger than the case without the AGB yields (dashed lines) and much closer to the observational data (Cunha et al. 2003). Note that the F yields from AGB stars were increased with the new reaction rates (§2). Different from C, F is not significantly produced by SNe II/HNe according to our yields, and thus [F/Fe] rapidly decreases from [Fe/H] ~ -1 to ~ -3. Therefore, the F abundance is a good clock to distinguish the contribution from low-mass AGB stars and supernovae. We should note, however, that the F yields from supernovae may be increased by a factor of ~ 1000 by the ν-process (Izutani, Umeda, & Yoshida 2010, private communication; see also Woosley & Weaver 1995). The effect of rotating massive stars is uncertain since F yields are not available in the literature.

These results are consistent with the models that adopt the same supernova and AGB yields in Romano et al. (2010, hereafter R10). There are some differences, for example, for elements heavier than N, our results fall between Models 4 and 5 in R10 because we adopt an hypernova efficient of $\epsilon_{\rm HN} = 0.5$. The C and N abundances are predicted to be higher in Models 4 and 5 than our results because the low and intermediate-mass star yields of van den Hoek & Groenewegen (1997) were used. In Model 15 of R10, the same AGB yields are adopted as in our models, but the C and N abundances are still higher. This may be due to the addition of the Geneva pre-supernova yields along with the supernova yields from K06. We note that rotation changes the pre-supernova structure and thus should also change the nucleosynthesis during the explosion. Hence to be fully self consistent, supernovae yields computed from a rotating pre-supernova structure should be included but

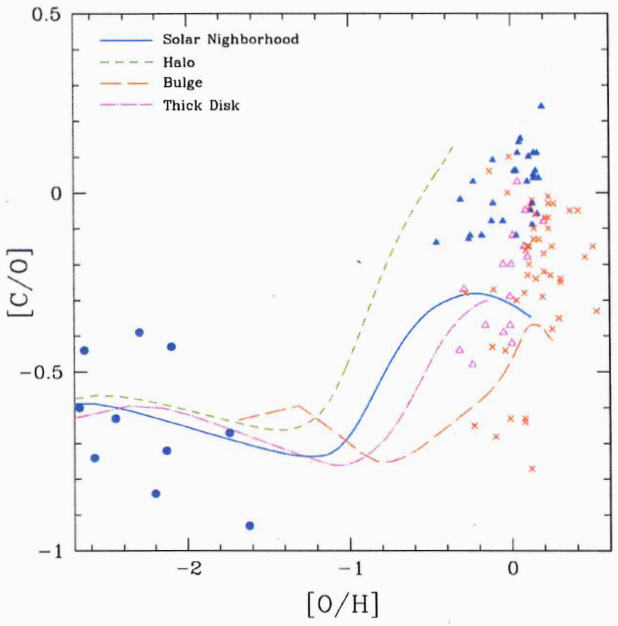

Figure 15. Evolution of the [C/O] ratio against [O/H] for the solar neighbourhood (solid lines), halo (short-dashed lines), bulge (long-dashed lines), and thick disk (dot-dashed lines) with AGB yields. The observational data sources are: filled circles, unmixed stars in Spite et al. (2006); filled triangles and open triangles, Bensby & Feltzing (2006) for thin and thick disk stars, respectively; crosses, Lecureur et al. (2007) for bulge stars.

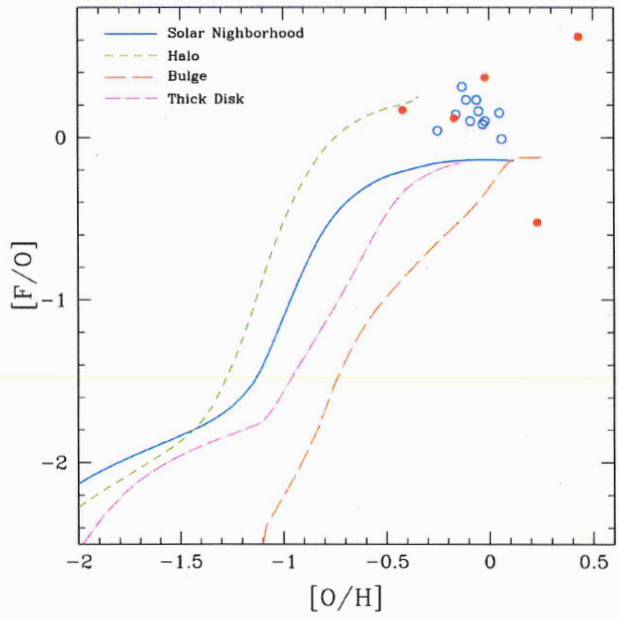

Figure 16. The same as Fig. 15 but for the [F/O] ratio. The observational data sources are: open circles, Cunha et al. (2003) for the solar neighbourhood stars; filled circles, Cunha, Smith, & Gibson (2008) for bulge stars.